

Crack Path Selection in Orientationally Ordered Composites

Atoallah Mesgarnejad^a, Chunzhou Pan^b, Randall M. Erb^b, Sandra J. Shefelbine^{b,c}, Alain Karma^{a,*}

^a*Center for Inter-disciplinary Research on Complex Systems, Department of Physics, Northeastern University, Boston, MA. 02115, U.S.A.*

^b*Department of Mechanical and Industrial Engineering, Northeastern University, Boston, Massachusetts 02115, USA*

^c*Department of Bioengineering, Northeastern University, Boston, Massachusetts 02115, USA*

Abstract

While cracks in isotropic homogeneous materials propagate straight, perpendicularly to the tensile axis cracks in natural and synthetic composites deflect from a straight path, often increasing the toughness of the material. Here we combine experiments and simulations to identify key emergent properties that predict whether cracks propagate straight or kink on a macroscale larger than the composite microstructure. Those properties include the anisotropy of the fracture energy, which we vary several folds by increasing the volume fraction of orientationally ordered alumina platelets inside a polymer matrix, and a microstructure-dependent process zone size that modulates the additional stabilizing or destabilizing effect of the non-singular stress acting parallel to the crack. Those properties predict the existence of an anisotropy threshold for crack kinking and explain the surprisingly strong dependence of this threshold on load distribution.

Keywords: Fracture, Ceramic composites, Orientationally ordered materials

*Corresponding author

1. Introduction

In natural and synthetic composites consisting of hard particles within a soft matrix, crack path prediction is a complex, intrinsically multiscale, problem. Accurate prediction of crack paths, especially the existence of kinking, provides insight into the properties of fracture toughness and strength. Therefore, understanding how cracks propagate at the scale of the hard particles (microscale) and at the scale much larger than the particles (macroscale) are both essential. On the microscale, cracks can either penetrate or be deflected by the hard particles depending on the elastic and fracture properties of the two phases [1, 2, 3]. Such microscale deflection has been hypothesized to provide an apparent toughening mechanism in both natural [4, 5, 6, 7] and biomimetic [7, 8] composites by greatly increasing the fracture surface area and the required energy to fracture the material. Crack deflection at the microscale is considered well understood. Microscale deflection can potentially, but not always, lead to macroscale crack deflection even in pure tensile (mode-I) loading configurations which has been studied extensively in both natural [9, 10] and biomimetic composites [7, 11]. For example macroscale kinking occurs in healthy bone for cracks perpendicular to the collagen fiber direction while straight crack propagation has been seen in pathological bone exhibiting disordered collagen fibers [10]. Other microstructurally ordered natural composites that have impressive fracture toughness and macroscale crack kinking include seashells [12, 13, 14], wood [15, 16], dental enamel [17], and rock [18, 19]. While these observations suggest that macroscale crack kinking may result from microscale alignment, other structural heterogeneities such as modulus variations and porosities in natural composites may also contribute to kinking [9].

In synthetic composites, in which other heterogeneities can be minimized, micro-sized particles or fibers are added to concrete [20], ceramics [21, 22], and polymers [23] to increase toughness. The particles or fibers in synthetic composites are often not arranged at the micro-structural level as they are in natural materials and can show crack kinking [9, 13] as well as straight crack propagation [10]. When the micro-structure is well-aligned, such as in freeze-casted nacre-like alumina samples, and subjected to notched three-point bending, crack kinking occurs when the crack direction is perpendicular to the microstructure orientation [24]. 3D printed composites have also shown crack kinking both with aligned microstructure [25] and macrostructures [7].

Previous experiments on natural and synthetic composites have explored

the influence of anisotropy on crack path, where they have found that crack deflection depends on fracture toughness anisotropy, the direction of the crack relative to the aligned microstructure, and the volume fraction of the particles [26]. These studies have developed regression models to predict the kink angle [26], estimated a critical anisotropy ratio for crack kinking [27], and developed a geometric adjustment factor for samples with fiber direction perpendicular to the crack direction [26]. In the present work, we use a rather unique composite system that allows us to vary the fracture energy anisotropy several fold while keeping the elastic properties nearly isotropic. Therefore, we are able to investigate the effect of the fracture energy anisotropy on crack paths on a macroscale (i.e. with both the fracture energy and the crack paths measured on a sample scale much larger than the composite microstructure). This is achieved by leveraging magnetic alignment to produce highly oriented and homogeneous alumina microstructures within photocurable polymers. By conducting Mode I tensile testing of notched specimens with these composites in different geometries that promote or suppress kinking, we are able to quantify experimentally the fracture energy anisotropy and, at the same time, to demonstrate a surprisingly strong effect sample geometry on crack kinking behavior.

Furthermore, to explain our experimental findings, we use the phase-field approach for fracture [28, 29, 30]. This method has been validated by theoretical analyses [28, 31] and comparisons with observed crack paths in benchmark geometries [32]. It has been used to model a wide range of fracture phenomena in diverse applications including thin-film fracture [33], thermal fracture [34], mixed mode fracture [35], chemo-mechanical fracture [36, 37, 38, 39], dynamic fracture [35, 40, 41], fracture in colloidal systems [42], as well as ductile fracture [43, 44, 45, 46] and fatigue crack growth [47, 48, 49]. Directly relevant to the present study, the phase-field method has also been used to model brittle fracture with an anisotropic fracture energy [50, 51, 31] and fracture of composites at micro [52, 53, 54] and macro [55, 56] scales. Here, we perform phase-field simulations that demonstrate the existence of a transition from straight to kinked crack propagation on a macro scale with increasing magnitude of the fracture energy anisotropy in good quantitative agreement with experimental findings. Simulations also reproduce the surprisingly strong effect of sample geometry on crack kinking behavior for values of the process zone size in the phase-field model estimated from experimentally measured mechanical properties. We explain qualitatively this effect in terms of the singular T-stress acting parallel to the

crack that is known to influence crack path selection in isotropic media such as PMMA [57]. The combined experimental and numerical results provide a comprehensive understanding of the combined effects of fracture energy anisotropy and sample geometry on macroscale crack paths in anisotropic composites.

2. Materials and Methods

2.1. Preparation of oriented Alumina-reinforced polymer matrix composites

For the experiments, we used composites with varying volume fraction f_v of uniformly dispersed micron-size alumina platelets embedded in a polymeric matrix that exhibited little plastic deformation. Platelets were dispersed within uncured polymeric resin and then forced to orient in a common plane by applying a magnetic field, thereby producing a composite with a fine microstructure with long-range orientational order. To produce the polymer matrix, we mixed two photocurable resins, *EBECRYL 230* urethane acrylate and isobornyl acrylate, with a weight ratio of 1:9 so as to raise the viscosity and prevent the sedimentation of particles, together with two photoinitiators (*1-Hydroxycyclohexyl phenyl ketone* and *Phenylbis phosphine oxide*, 1 wt% each relative to the resin). To this, magnetized alumina particles were added at 0–7 Vol% ($f_v = 0 - 0.07$).

To produce the magnetized Alumina particles, first 10 g of 7.5 μm alumina (Antaria, Australia) micro-platelets were dispersed in 400 mL of deionized water in an Erlenmeyer flask with a magnetic stirring bar stirring at 500 rpm. The pH of the water was maintained as 7 under room temperature to keep a positive charge on the alumina surface (isoelectric point at $\text{pH} \approx 9$). Separately, 375 μL of super paramagnetic iron oxide nanoparticles (SPIONS, EMG 705, Ferrotec, Nashua, NH) were diluted with 40 mL of deionized water. The diluted dispersion was added dropwise into the suspension with alumina particles. The negatively charged SPIONs electrostatically coated the positively charged alumina micro-platelets. Typically, the adsorption was complete within 24 hours as was determined when the supernatant liquid was transparent. The magnetized alumina was isolated through vacuum filtration in a Buchner filter. The particles were dried in an oven at 60 $^\circ\text{C}$ for at least 12 hours and were stored in a desiccator chamber with a humidity below 10%.

Urethane (*EBECRYL 230*, Allnex) and isobornyl acrylate (*IBA*, Sigma Aldrich) were mixed with a weight ratio of 1:9. The two resins were made

photo-curable by adding both 1-hydroxycyclohexyl phenyl and (Sigma Aldrich) phenylbis (2,4,6-trimethylbenzoyl) phosphine oxide (Sigma Aldrich) as photo initiators at a weight ratio of 1% each. The resin was mixed with a spatula and sonicated for 1 min. Magnetized alumina at defined volume fractions was then added and dispersed with an ultrasonic probe (Sonifier 250, Branson) for 2 min with output power 2 and duty circle of 20. The solution was transferred to sonicate bath for another 20 min sonication to further ensure that the magnetized alumina is homogeneously dispersed in the polymer resin. The sonicated solution was then spread onto a glass slide by a transfer pipet and covered by another glass slide with a photomask to form a sandwich mold. The glass slide and the photomask were separated by 0.3 mm thick glass spacers (see Fig. 1).

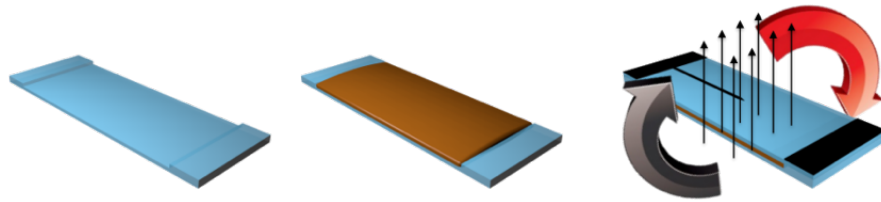


Fig. 1: Composites fabrication: glass slide with two glass spacers at each ends (left), resin spread on the glass slide (middle), resin covered by the glass slide with photomask and placed in the oscillating field (right).

The mold was then placed into an oscillating magnetic field created by solenoids powered with current controllers that were themselves controlled by a LabVIEW [58] program. The oscillating field consisted of a constant vertical field (Z-field) of 140 G and a dynamic horizontal field (X-field) that was a 1.5 Hz sinusoidal field with a peak field of 240 G. Due to the ultrahigh magnetic response, the magnetized alumina could be aligned within the X-Z plane in 10 seconds. After magnetized alumina was assembled, ultraviolet (UV) light emitted from a UV lamp (6 W, 365 nm) was applied 10 cm above the sample curing the unmasked area. Samples with different volume fraction of alumina micro-platelets required different curing time to obtain a testable thickness. Typically, exposure of 17 s, 23 s, 35 s, 50 s, 60 s, 70 s, 75 s, and

90 s was required to cure 0%, 1%, 2%, 3%, 4%, 5%, 6%, 7%, and 10% filled samples, respectively. Next, the mold was carefully peeled apart leaving the sample stuck to the glass slide with the photomask. The surface of the sample was cleaned by isopropanol (IPA, Sigma-Aldrich) and was then flipped over and subjected to the same UV light for 1 min of short post-curing before it was peeled off by a razor blade and transferred to a container. For further post-curing, the light of a digital light processing (DLP) projector placed 25 cm away from the sample was used to post cure each side of the sample for 15 min. Afterwards, the notch position was marked 1 mm ahead of the tip before the sample was placed in an oven at 90 °C. The notch was made by a sharp razor blade after the sample was heated for 20 min and became soft. The notched sample was further heat treated in the oven at 90 °C for another 2 hours to relax the residual stress that may have been created at the crack tip during notching. During the heat treatment, glass slides were used to cover the sample to prevent warping.

2.2. Characterization of particle dispersion in experimental samples

To visualize the microstructure, fabricated composites were freeze fractured in liquid nitrogen to expose a cross-section without any plastic deformation. These cross-sections were observed in a scanning electron microscope (SEM) as shown in Fig. 2a and Fig. 2b for samples with \parallel (0°) and \perp (90°) platelet orientations, respectively. Investigation of the microstructure shows that the ceramic platelets are homogeneously distributed with average nearest neighbor separation, $\langle r \rangle$, around 11 μm . This inter-particle-spacing was established through analytic predictions and graphical analysis. We calculated the pair correlation (radial distribution) function, $g(r)$, for the platelets by graphically identifying platelet centers in the 90° case using ImageJ [59] analysis software supplied by the NIH, shown in Fig. 2c. The pair correlation indicates that there is almost no correlation between particle positions in long or short range, indicating that there is no clustering or ordering. In other words, the alumina is randomly and homogeneously distributed. It should be noted that $g(r)$ can therefore not be relied upon to establish nearest neighbor distances. We investigated nearest neighbor distance using the analytical expression for homogeneous particle suspensions $\langle r \rangle \simeq (V_p/f_v)^{1/3} = n^{-1/3}$ where V_p is a single platelet's volume, and $n = f_v/V_p$ is the platelet number density. To calculate the platelet number density, n , we assumed that the platelets were discs with volume $V_p = \pi a^2 t$, where the platelet diameter was $a = 7.5 \mu\text{m}$ and thickness was $t = 0.3 \mu\text{m}$. The analytically calculated near-

est neighbor separation $\langle r \rangle$ is dependent on the platelet volume fraction as shown in Fig. 2d. For the 4% volume fraction sample shown in Fig. 2, the analytic equation predicts roughly $\langle r \rangle \sim 11 \mu\text{m}$. To verify this prediction, and since we are unable to use $g(r)$, we employed a custom algorithm to calculate the average distance to the nearest neighbor from each particle over a variable angular resolution. This algorithm is depicted in Fig. 2e in which only the closest particle over a scan across an angle of α is considered. All of the closest particles are then averaged over 360° . This approach produces the results shown in Fig. 2f for different angular resolutions of α . To avoid edge effects, boundaries are made periodic by arraying particle positions in x and y . This algorithm indicates the separation between nearest neighbors is $\langle r \rangle \sim 14 \mu\text{m}$ indicating a reasonable agreement with the analytical model.

2.3. Mechanical testing procedures and crack path mapping

Using our composites, we conducted Mode I tensile testing experiments of notched specimens in the two different geometries depicted in Fig. 3 with platelets oriented at different angles (α_Γ) with respect to the horizontal axis perpendicular to the tensile direction. For shorthand notation, we refer to $\alpha_\Gamma = 0$ and $\alpha_\Gamma = \pi/2$ as perpendicular (\perp) and parallel (\parallel) orientations, respectively. The \parallel orientation has a smaller fracture energy than the \perp orientation and produces straight propagating cracks for both the short and long sample geometries. In addition, the short sample geometry suppresses kinking entirely for the \perp orientation. It can therefore be used to measure experimentally the fracture energy for straight propagating cracks for both the \parallel and \perp orientations and to quantify the fracture energy anisotropy as described in section 2.4. In contrast, the long sample geometry promotes kinking for the \perp orientation and is used to study the effect of the magnitude of the fracture energy anisotropy on crack path selection. Mode I loading was produced by symmetrically gripping the samples at two opposite boundaries as commonly done in polymeric [60] and biological [61] materials. The samples were mounted in tensile grips of a universal tester (Instron-5966 with 500 N load cell) with a data recoding frequency of 10 Hz. The gripping regions are shown by the gray areas in Fig. 3. Care was taken to ensure the grip configuration and clamping force did not play a role in the measured properties propagating cracks far from the clamps.

During the tensile loading, the bottom clamp remained fixed while the top clamp raised up at 20 mm/min. For long samples, the out of plane

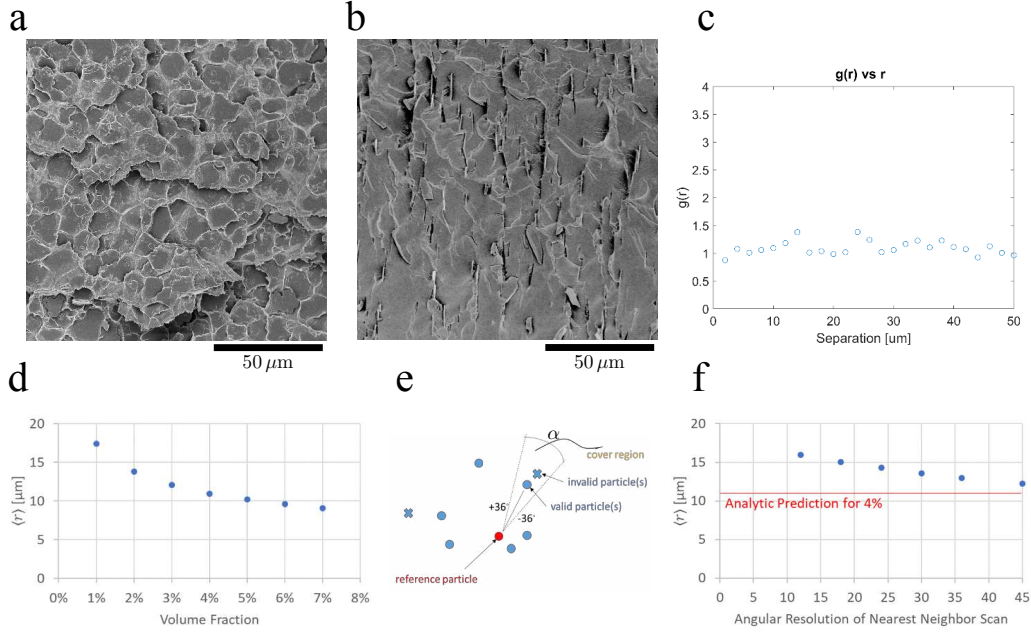


Fig. 2: **a-b**, SEM cross-sections taken from fractured samples reinforced with 4% alumina oriented \parallel (**a**) and \perp (**b**, obtained from freeze fracture to avoid kinking). **c**, Plot of the pair correlation (radial distribution) function, $g(r)$ vs. platelet separation r calculate using graphically identified platelets in a \perp sample. **d**, Analytical prediction of nearest neighbor spacing using the relationship $\langle r \rangle \sim n^{-1/3}$. **e**, Schematic of the algorithm for locating nearest neighbors with a certain angular resolution, α , disregarding more distant particles. **f**, Results of the custom algorithm showing a slight dependence on the angular resolution, but being in reasonable agreement with the analytical expression for a volume fraction of 4%.

motion was partially restrained by two glass slides separated by 1 mm. Our experimental observations (in both short and long samples) verify that the clamping did not introduce mode-II at the crack tip and only influenced the kinking through change of the T-stress. In both phase-field simulations and experiments, small deviations can have either small positive ($\theta^* > 0$) or negative ($\theta^* < 0$) angles, confirming that there is no bias.

The crack propagation was captured by a mounted phone camera with a recording ratio of 30 frames/second. After the test, an image of the cracked sample was taken with a 1 cm grid paper underneath it. The crack shape was measured in ImageJ [59] (Fig. 4). The coordinates of the dots were quantified and mapped into a new coordinate system with the origin located

at the notched front. We calculate the emergent angle of cracks as the linear fit to the first 2 mm of the crack path.

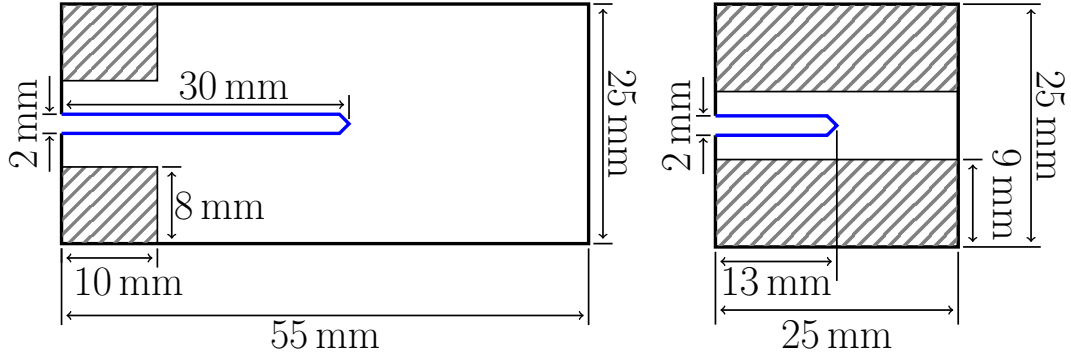


Fig. 3: Long (left) and short (right) samples. The gray areas were mounted in Instron grips.

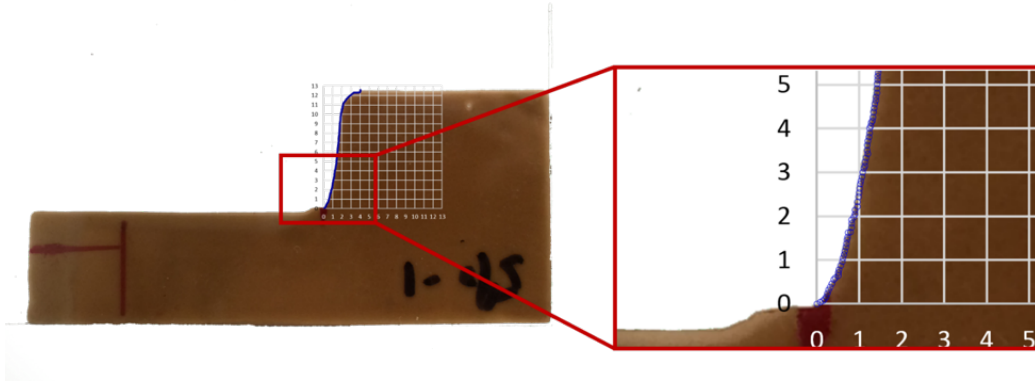


Fig. 4: Measuring the crack path showing how the experimental crack was path scanned.

2.4. Estimation of fracture toughness and elastic modulus anisotropies

The short samples geometry and loading configuration allows us to estimate the fracture toughness from the critical imposed displacement at which sample breaks. The short sample geometry can be thought as a $L_x \times L_y$ domain with a crack that extends from $-L_x/2$ to l_c under constant displacement $u = (0, \delta)$ at $y = L_y$ and fixed at $y = 0$. Since the loading is uniform

we can assume that vertical strain is almost constant in front of the crack *i.e.*, $e_{yy} = \delta/L_y$. Moreover, for a slender geometry $L_x > L_y$ we can assume $e_{xx} = 0$ far from the right hand side boundary. Therefore we can write the elastic energy per unit thickness in front of the crack as

$$\mathcal{B}(l_c) = \frac{1}{2} \int_{l_c}^{L_x/2} \int_0^{L_y} \sigma_{yy} e_{yy} dy dx = \frac{\delta^2(\lambda + 2\mu)}{2} \frac{(L_x/2 - l_c)}{L_y} \quad (1)$$

where for elastic modulus E and Poisson's ratio ν , $\lambda = E\nu/(1 - \nu^2)$ and $\mu = E/2(1 + \nu)$ are Lamé constants for a thin sample (*i.e.*, in plane stress).

The energy release rate by definition is the negative change of the elastic energy due to change of the crack length (in 2D and for prescribed displacement) *i.e.*,

$$G = - \left. \frac{\partial \mathcal{B}}{\partial l_c} \right|_{\delta=const} = \frac{\lambda + 2\mu}{2} \frac{\delta^2}{L_y} \quad (2)$$

and therefore at onset of (straight) propagation, where the load is at its maximum $f = f_{\max}$ and the imposed displacement at that instance is δ_c (see Fig. 8a), we can write the fracture toughness as

$$\Gamma = \frac{\lambda + 2\mu}{2} \frac{\delta_c^2}{L_y} \quad (3)$$

A similar estimate can be made by a conservation of energy argument (see (5)) assuming that the energy stored before the onset of the propagation ($l_c = 0$) is spent on the creation of new fracture surfaces *i.e.*,

$$\Gamma = \frac{\mathcal{B}(0)}{L_x/2} = \frac{(\lambda + 2\mu)}{2} \frac{\delta_c^2}{L_y} \quad (4)$$

We used (3) to estimate the fracture toughness of the pure polymer matrix and 5% \perp samples from their associated load-displacement curves (see Fig. 8a) reported in Table 1. To perform the calculation (and associated error analysis), we used the elastic modulus measured in independent uniaxial measurements (Table 1).

To calculate the anisotropy of the elastic modulus (*i.e.*, E_{\perp}/E_{\parallel}) and fracture toughness (*i.e.*, $\Gamma_{\perp}/\Gamma_{\parallel}$), we used the experimentally measured load displacement curves (see Fig. 8a for example). We can think of our experimental specimens as complex springs where their stiffness S only depends on the

sample geometry, loading configuration, and elastic properties. When the crack propagates, the resultant force drops since the sample becomes more compliant. Therefore, at the onset of fracture, the load is at its maximum $f = f_{\max}$ where we signify the imposed displacement at that instant as δ_c . To calculate the stiffness of the sample, we fit the load per unit thickness f/h of the sample (where h is the sample thickness) vs. its imposed boundary displacement δ for $\delta < 0.1$ mm linearly. This limit was chosen such that it is always below the critical imposed displacement δ_c for all performed experimental measurements. *i.e.*, the load per unit thickness h is a linear function of the imposed displacement before the cracks propagate when $\delta < \delta_c$

$$\frac{f}{h} = S\delta \quad \delta < \delta_c \quad (5)$$

The stiffness of the samples changes with changing f_v but, for given f_v , the slopes of load displacement curves for the \perp and \parallel samples remain almost constant, which allows us to treat these samples in both \perp and \parallel directions as isotropic.

Next we show that the fracture toughness anisotropy can be calculated from the work to fracture. Due to energy conservation, we can write the energy stored per unit thickness \mathcal{B} in terms of the imposed displacement δ and the resultant force f in short samples (before the cracks advance) as

$$\mathcal{B}(\delta) = \int_{\Omega} \mathcal{W}(u) dx = \frac{1}{2} \int_0^{\delta} \left(\frac{f}{h} \right) d\delta \quad (6)$$

here $\mathcal{W}(u) = (C_{ijkl}e_{ij}e_{kl})/2$ is the elastic energy density where $C_{ijkl} = \lambda\delta_{ij}\delta_{kl} + \mu(\delta_{il}\delta_{jk} + \delta_{ik}\delta_{jl})$ is the linear elastic constitutive tensor and $e_{ij} = (u_{i,j} + u_{j,i})/2$ is the linear strain.

Since in ideally brittle materials fracture is the only dissipating mechanism, we can estimate the fracture toughness by matching the energy $h\mathcal{B}(\delta_c)$ released when the crack breaks the sample in two to the energy Γhl_c needed to create the crack of length l_c , which yields

$$\mathcal{B}(\delta_c) = \Gamma l_c \quad (7)$$

Therefore, we can write the ratio of the \perp and \parallel fracture toughnesses as

$$\frac{\Gamma_{\perp}}{\Gamma_{\parallel}} = \frac{\gamma_{f\perp}}{\gamma_{f\parallel}} \quad (8)$$

where the different subscripts correspond to different orientations of platelets and we define the work to fracture per unit thickness as γ_f as the area of load per unit thickness vs. displacement curve

$$\gamma_f = \int_0^{\delta_c} \left(\frac{f}{h} \right) d\delta \quad (9)$$

Thus, the straight crack propagation for both \perp and \parallel in the short samples (see Fig. 6) enables us to accurately measure the anisotropy of fracture toughness from the measured load-displacement curves (*e.g.*, Fig. 8a).

2.5. Phase field modeling

The phase-field model couples the elastic displacement field $u = (u_x, u_y)$ to a scalar phase field ϕ that varies smoothly from $\phi = 1$ in the pristine material to $\phi = 0$ in the fully broken material over a length scale ξ , which sets the size of the process zone around the crack tip where linear elasticity breaks down. The total energy of the system is described by the functional

$$\begin{aligned} \mathcal{F}_{\xi}(u, \phi) = & \int_{\Omega} g(\phi) \mathcal{W}(e(u)) dx \\ & + \frac{\Gamma_{\perp}}{4C_{\phi}} \int_{\Omega} \left(\frac{w(\phi)}{\xi} + \xi A_{ij} \partial_{x_i} \partial_{x_j} \phi \right) dx \end{aligned} \quad (10)$$

where the first and second terms on the right-hand-side correspond to the elastic strain energy and the anisotropic fracture energy [31], respectively. We define the fracture energy anisotropy matrix as

$$\hat{A} = \begin{bmatrix} \mathcal{A}^{-2} & 0 \\ 0 & 1 \end{bmatrix} \quad (11)$$

$$A_{ij} = Q_{ik} \left(\frac{\pi}{2} - \alpha_{\Gamma} \right) Q_{jl} \left(\frac{\pi}{2} - \alpha_{\Gamma} \right) \hat{A}_{kl} \quad (12)$$

where Q is the rotation matrix, and we denote by α_{Γ} the angle between the plane of the platelet and the horizontal axis such that $\alpha_{\Gamma} = 0^{\circ}$ and

$\alpha_\Gamma = 90^\circ$ correspond to the \parallel and \perp orientations, respectively. With the choice $C_\phi = \int_0^1 \sqrt{w(\phi)} d\phi$, the fracture energy is Γ_\perp for propagation along the x direction parallel to the parent crack and perpendicular to the platelet faces and $\Gamma_\parallel = \Gamma_\perp/\mathcal{A}$ for propagation along y parallel to the faces. In general, Eq. (10) results in an anisotropic fracture energy of the form [31]

$$\Gamma(\theta) = \Gamma_\perp \sqrt{\mathcal{A}^{-2} \sin^2(\theta + \alpha_\Gamma) + \cos^2(\theta + \alpha_\Gamma)} \quad (13)$$

Furthermore, $\mathcal{W}(e(u))$ is the elastic energy density defined for isotropic linear elastic solid as $\mathcal{W}(e(u)) = (\mathcal{C}_{ijkl} e_{kl}(u) e_{ij}(u))/2$ where $e_{ij}(u) = (\partial_{x_j} u_i + \partial_{x_i} u_j)/2$ is the strain tensor and the elastic constitutive tensor for plane-stress elasticity is given as $\mathcal{C}_{ijkl} = \lambda \delta_{ij} \delta_{kl} + \mu (\delta_{il} \delta_{jk} + \delta_{ik} \delta_{jl})$ where $\lambda = E\nu/(1 - \nu^2)$ and $\mu = E/(2(1 + \nu))$ are the Lamé coefficients for elastic modulus E and Poisson's ratio ν .

In addition, we use the specific forms of the function $g(\phi) = 4\phi^3 - 3\phi^4$ and $w(\phi) = 1 - g(\phi)$ [29, 31] to model the propagation of a fracture from a single flaw by prohibiting the initiation of new cracks in the undamaged ($\phi = 1$) material. All simulations are performed in 2D plane stress using the classic iterative minimization for quasi-static crack propagation [30], which consists of finding the minimizers of \mathcal{F}_ξ by solving the Euler-Lagrange equations for (10). The Euler-Lagrange equations derived variationally from Eq. (10) are discretized using the Galerkin finite element method and solved using distributed data structures provided by libMesh [62] and linear algebra solvers in PETSc [63, 64]. The sample geometries depicted in Fig. 3 are meshed using a triangular Delaunay mesh with average edge size $\approx 27.5 \mu\text{m}$. To perform the numerical simulations, we imposed the boundary conditions associated with the grips as $u_x = 0, u_y = \pm\delta$ on all nodes in contact with the grips (*i.e.*, the gray shaded areas in Fig. 3 and Fig. 8a) and the sharp notch was simulated by imposing $\phi = 0$ at the tip of the v-shaped notch. Typical simulation included ≈ 500 kDOFs and was ran on 40 physical cores of 2.2 GHz Intel Xeon E5-2630 CPU for ≈ 24 hr. Simulations are carried out with the estimate $\nu = 0.2$, and the input parameters \mathcal{A} and ξ .

Finally, we calculate the initial kink angle θ^* by measuring the angle of the line that connects the crack tip to the initial notch tip at the first time step where the crack is propagated a distance larger than 2ξ . The standard deviation of measurement is calculated as the maximum change in angle as the result of discretization.

2.6. Dimensional analysis of the phase-field model

Since accurate values of the fracture toughnesses Γ_{\perp} and Γ_{\parallel} cannot be calculated directly from the experimental measurements, we show in this section that the crack path is only affected by the ratio of these energies (the fracture toughness anisotropy $\mathcal{A} = \Gamma_{\perp}/\Gamma_{\parallel}$) and not their individual values. If we define the dimensionless coordinates $\bar{x} = x/L$ (where we choose L to be the sample width), dimensionless displacement $\bar{u} = u/\sqrt{\Gamma_{\perp}L/E}$, and dimensionless elasticity tensor $\bar{\mathcal{C}} = \mathcal{C}/E$, using Eq. (10) we can write the dimensionless energy as

$$\begin{aligned} \bar{\mathcal{F}}_{\xi}(\bar{u}, \phi) = \frac{\mathcal{F}_{\xi}(\bar{u}, \phi)}{\Gamma_{\perp}} &= \int_{\Omega} g(\phi) \bar{\mathcal{W}}(e(\bar{u})) d\bar{x} \\ &+ \frac{1}{4C_{\phi}} \int_{\Omega} \left(\frac{w(\phi)}{\bar{\xi}} + \bar{\xi} A_{ij} \partial_{\bar{x}_i} \partial_{\bar{x}_j} \phi \right) d\bar{x} \end{aligned} \quad (14)$$

where $\bar{\mathcal{W}}(e(\bar{u})) = \bar{\mathcal{C}}_{ijkl} \bar{e}_{kl}(\bar{u}) \bar{e}_{ij}(\bar{u})/2$, $\bar{e}_{ij}(\bar{u}) = (\partial_{\bar{x}_j} \bar{u}_i + \partial_{\bar{x}_i} \bar{u}_j)/2$, and $\bar{\xi} = \xi/L$. Therefore it is easy to see that the crack path predicted by this model only depends on the sample geometry and loading configuration, the relative size of process zone with respect to the sample size ξ/L , Poisson's ratio ν , and the fracture energy anisotropy $\mathcal{A} = \Gamma_{\perp}/\Gamma_{\parallel}$.

3. Results

3.1. Experimental results for \parallel and \perp platelet orientations

Fig. 5 shows the results of Mode I fracture experiments in different geometries with \parallel and \perp platelet orientations and volume fraction of platelets f_v from 0 to 0.07. In the long sample geometry, crack kinking occurs with perpendicular oriented platelets for sufficient volume fraction, while in the short sample cracks propagate straight across for all volume fractions in this range. Examination of crack paths on a microscale (Fig. 5 right columns) revealed that the crack front did not penetrate the platelets that are orders of magnitude stronger and stiffer than the matrix as shown in Table 1. As a result, the crack front propagated around platelets following a tortuous microscale path. Examination of crack paths on a macroscale (shown in Fig. 6 and quantified in Fig. 7) revealed that, for the \perp orientation, cracks propagated straight in all short samples over the range of volume fraction $f_v \leq 0.07$ (Fig. 7), despite being sporadically deflected on a microscale (see Fig. 5c right column). In contrast, in long samples cracks exhibited a clear transition from

straight to kinked propagation over the same range of f_v . Several experiments were conducted in both sample geometries to show that crack paths were highly reproducible. Those observations demonstrate that microscale crack deflection, common in composites with hard particles embedded in a softer matrix, is not generally a sufficient condition for macroscale deflection, which depends in a non-trivial way on both the microstructure (f_v) and sample/loading geometry.

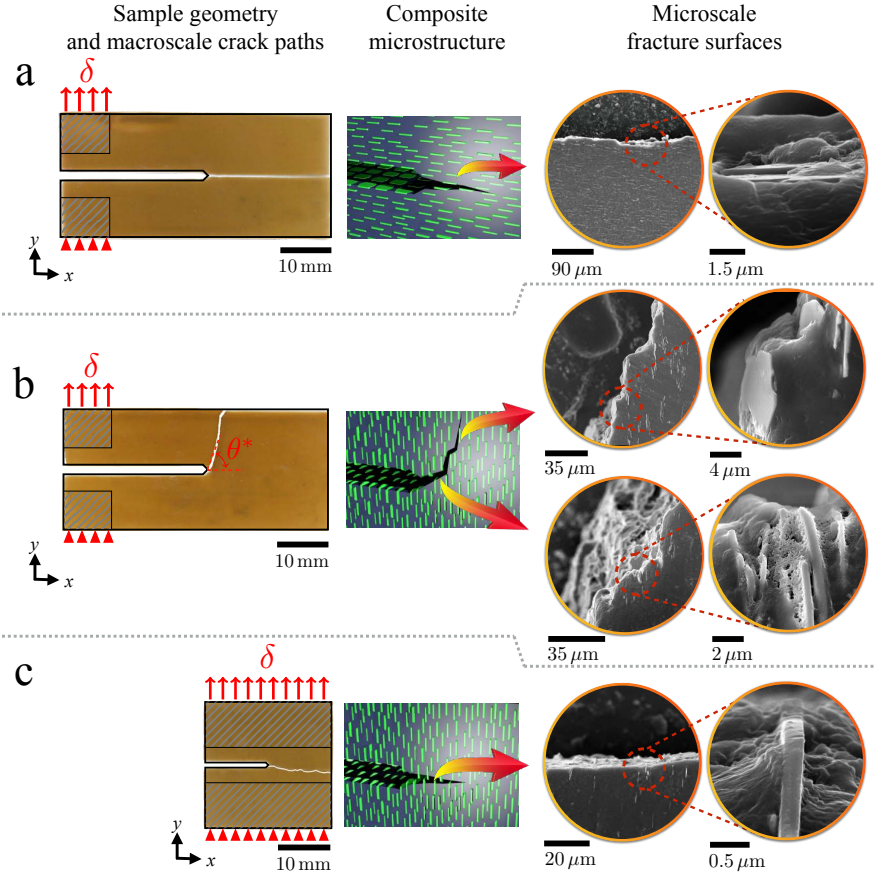


Fig. 5: Results of pure tensile fracture experiments for 5% platelet volume fraction bicomposites illustrating stark differences between microscale and macroscale crack paths and the strong influence of sample geometry on macroscale paths. The left column shows the macroscale crack paths in fractured samples for different platelet orientations illustrated in the middle column and the right column shows SEM images of microscale crack paths at different magnification. **a**, Long sample with platelets oriented parallel to the crack propagation axis. The macroscale crack path is straight and the microscale fracture path travels along the platelet faces. The same behavior is observed in short samples (results not shown). **b**, Long sample with platelets oriented perpendicular to the crack propagation axis. The macroscale crack path is strongly kinked and the microscale fracture path travels along a staircase with vertical sections parallel to the platelet faces (top two images of right column) and horizontal sections perpendicular to the faces (bottom two images of right column). **c**, Short sample with the same platelet orientation as in **b**. In contrast to **b**, the macroscale crack path remains straight even though the platelets deflect the crack on a microscale. Platelets do not break and deflect cracks on a microscale in all samples.

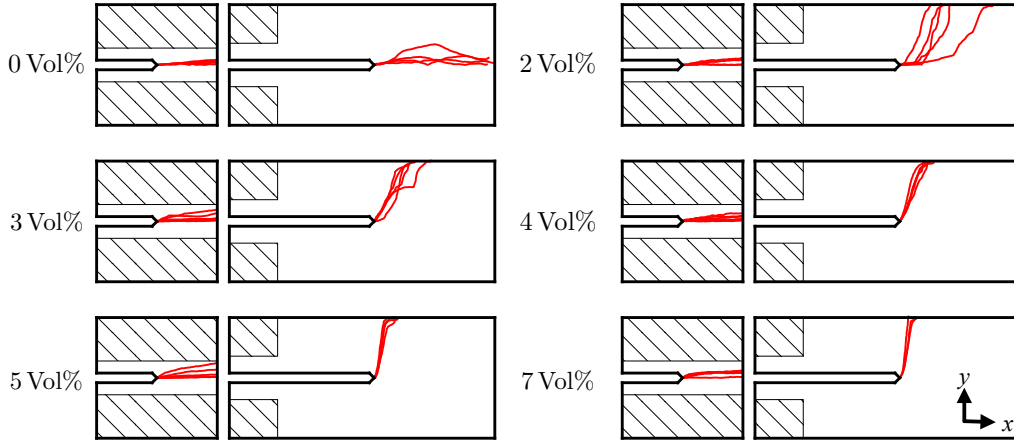


Fig. 6: Experimentally observed macroscale crack paths in short and long samples for different volume fractions of alumina platelets oriented perpendicularly to the crack propagation axis (\perp orientation). The crack paths are digitized as shown in Fig. 4 and mirrored to $y > 0$ to show consistency of the initial crack kinking angle θ^* . Crack paths remain straight in all short samples but kink in long samples above a critical volume fraction of approximately 3%.

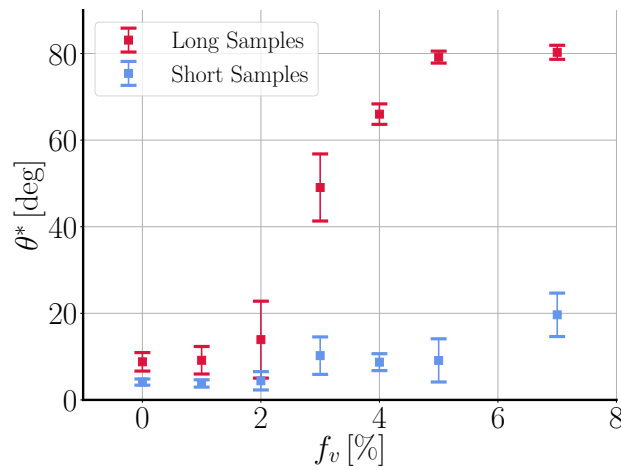


Fig. 7: Measured crack kinking angle θ^* from the experimental results in Fig. 6.

As a first step towards crack path prediction on a macroscale, we recorded load-displacement curves (Fig. 8a) to measure mechanical properties of com-

posites relevant for fracture, including the anisotropies of the fracture energy and elastic modulus respectively defined as the ratios $\Gamma_{\perp}/\Gamma_{\parallel}$ and E_{\perp}/E_{\parallel} of those quantities for the \perp and \parallel orientations. We used short samples in which cracks propagate straight on the macroscale, thereby allowing us to perform a direct measurement of $\Gamma_{\perp}/\Gamma_{\parallel}$ for all volume fractions, which is not feasible in long samples that exhibit kinking. E_{\perp}/E_{\parallel} was computed as the ratio of the slopes of the load-displacement curves for small displacements and $\Gamma_{\perp}/\Gamma_{\parallel}$ as the ratio of the areas under those curves up to fracture initiation. We note that the work to fracture, which is commonly used as an approximate measure of toughness [8, 65, 66], was not used here to measure the fracture energy for a given orientation, but only the ratio $\Gamma_{\perp}/\Gamma_{\parallel}$ for the \perp and \parallel orientations. Since the same short sample geometry is used to compute the areas under the force-extension curves for those two platelet orientations, and crack propagate straight in this geometry for $f_v < 0.07$ (thereby producing the same fracture surface area), the ratio of work to fracture is equal to the ratio of fracture energies for those two orientations as discussed in section 2.4. While those slopes measure the stiffnesses of the samples and generally depend on sample geometries, the ratio of stiffnesses for the \perp and \parallel orientations is identical to the ratio E_{\perp}/E_{\parallel} since identical geometries are used for both orientations. Results in Fig. 8d (Fig. 8(b-c) for individual measurements) show that, when f_v increases from 0 to 7%, $\Gamma_{\perp}/\Gamma_{\parallel}$ increases about 600% while E_{\perp}/E_{\parallel} only increases by about 20%. This suggests that the fracture energy anisotropy is predominantly responsible for crack kinking in long samples, but leaves open the question of why it is absent in short samples over the same range of f_v .

3.2. Phase-field modeling results for \parallel and \perp platelet orientations

To gain more insight into these results, we use the phase-field method [30, 29, 31] described in Section 2 to model crack paths on a macroscale using the experimentally measured fracture energy anisotropy and a quantitative estimate of the process zone size as input into the model. To estimate the process zone size, we performed independent measurements of material properties of the polymer matrix and 5% \perp composite using simple uniaxial tension. We chose the tensile axis parallel to the platelets corresponding to the \perp orientation in our fracture experiments. The elastic modulus E , tensile strength σ_c where measured using ASTM-D638V uniaxial tension test. In addition to above uniaxial tests, the fracture energy Γ_{\perp} of the matrix and the 5%

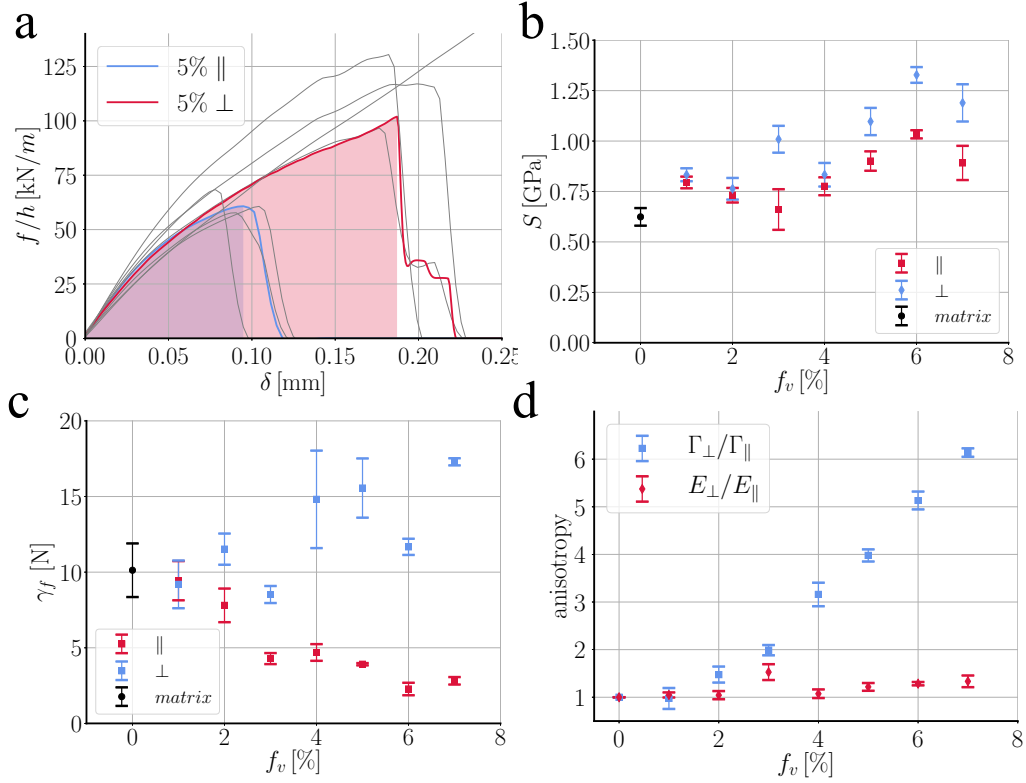


Fig. 8: **a**, Illustration of load-displacement curves used to measure the fracture energy anisotropy by exploiting the fact that cracks propagate straight in short samples for both \parallel and \perp platelet orientations. Curves for several 5 Vol% samples are shown as gray lines. Fracture occurs at higher load and displacement for the \perp orientation, reflecting a higher fracture energy. The colored lines and shaded regions illustrate the area under the curve used for the calculation of the fracture energy anisotropy for one \parallel sample (blue) and one \perp sample (red). **b**, Calculated stiffness of short samples for sample made of pure matrix as well as samples with \parallel and \perp platelet orientations. **c**, Estimated fracture energy from short samples for pure matrix as well as \parallel and \perp platelet orientations. **d**, Fracture energy anisotropy $\mathcal{A} = \Gamma_{\perp}/\Gamma_{\parallel}$ (blue) and elastic modulus anisotropy E_{\perp}/E_{\parallel} (red) along with their standard errors versus volumetric percentage of alumina platelets f_v over the whole range of f_v where cracks remain straight in short samples for both \parallel and \perp orientations.

composite was estimated based on value of imposed displacement at the onset of fracture δ_c in the experimental load-displacement curves of the short samples (see Section 2.4). Table 1 summarizes the measured elastic modulus E , tensile strength σ_c , and the fracture energy of different composite compo-

nents and the resulting composite. We further use the theoretical estimate $\xi \sim \Gamma_{\perp} E_{\perp} / \sigma_{c\perp}^2$ that follows from assuming that the maximum opening stress $\sigma_{yy} \sim K_I / \sqrt{\xi}$ at the crack tip is comparable to $\sigma_{c\perp}$.

Table 1: Independently measured elastic modulus E and maximum tensile strength σ_c , and calculated fracture energy estimate (see 2.4) along with their associated standard errors for the polymer matrix, and the 5% composite. The corresponding values reported for the Alumina platelets from [67].

Material	E [GPa]	σ_c [MPa]	Γ [kJ/m ²]
Alumina platelets [67]	380–410	210–500 [†]	0.022–0.095 [‡]
Polymer Matrix	0.444 ± 0.011	22.53 ± 0.78	0.84 ± 0.18
5% \perp Composite	0.603 ± 0.021	25.22 ± 0.97	1.6 ± 0.5
5% \parallel Composite	0.472 ± 0.08	14.16 ± 1.3	0.34 ± 0.06

[†] Flexural strength. [‡] Estimated from K_{IC}

The values of E and Γ only determine the physical magnitude of the imposed displacement $\delta \sim \sqrt{\Gamma L / E}$ that produces the applied tensile load, where L is the sample width, but do not affect the fracture behavior. The process zone size ξ is estimated by assuming that the maximum opening stress on the process zone scale $\sigma_{yy} \sim K_I / \sqrt{\xi}$ is comparable to the tensile strength of the material σ_c . Setting K_I equal to its value $K_{IC\perp} = \sqrt{\Gamma E}$ at the onset of propagation of a straight crack in short samples, yields the estimate $\xi \sim \Gamma E / \sigma_c^2$. By performing phase-field simulations we obtain the proportionality factor as

$$\xi \simeq 0.39 \frac{\Gamma E}{\sigma_{c\perp}^2} \quad (15)$$

A similar estimate has been previously obtained [68, 69] by a one-dimensional stability analysis of Eq. (10) for a broad class of functions $g(\phi)$ and $w(\phi)$ that did not include the present model. Combining Eq. (15) with our measurements of the elastic modulus and the ultimate tensile strength along with our estimate of fracture energy (compiled in Table 1), we estimate the process zone size as $\xi \simeq 285 \pm 126 \mu\text{m}$ for the polymer matrix, $\xi \simeq 309 \pm 115 \mu\text{m}$ for the 5% \parallel composite, and $\xi \simeq 593 \pm 207 \mu\text{m}$ for the 5% \perp composite (where \pm signs signify standard errors). For the matrix, this ξ estimate is comparable to the length of a craze region. For the composite, it is much larger than the

mean platelet spacing ($\simeq 10\mu\text{m}$) consistent with previous estimates that ξ is approximately 5–50 times larger than the microstructure scale in diverse composites [70]. We should also highlight that reduction in the process zone size ξ from \perp to \parallel roughly follows the prediction from our phase-field model *i.e.*, $\xi_{\perp}/\xi_{\parallel} = \mathcal{A}$. We use for all the computations $\xi = 225$ and $550\mu\text{m}$ as the lower and upper bounds of process zone size, respectively.

Since experimental samples are thin, we model fracture in 2D plane stress and focus on the crack-kinking \perp orientation. Moreover, since E_{\perp}/E_{\parallel} is weakly dependent on f_v , we assume that elasticity is isotropic and model the anisotropy of the fracture energy with the simple form [31] $\Gamma(\theta) = \Gamma_{\perp} \sqrt{\mathcal{A}^{-2} \sin^2(\theta) + \cos^2(\theta)}$ where θ (Fig. 9 inlay) is the angle between the crack axis and the reference straight propagation axis and $\mathcal{A} \equiv \Gamma_{\perp}/\Gamma_{\parallel}$ is the fracture energy anisotropy. This form is consistent with a 2D section of a transversely isotropic material where Γ is isotropic in the plane of the platelets and is symmetrical about the axis perpendicular to the platelets with maximum $\Gamma(0) = \Gamma_{\perp}$ and minimum $\Gamma(\pi/2) = \Gamma_{\parallel}$. Polar plots of Γ for different anisotropy values are shown in Fig. 9.

Fracture simulations were conducted for the same geometries studied experimentally (Fig. 5 left column) varying \mathcal{A} over the range (1 to 5) determined from experimental measurements of the fracture energy anisotropy around the kinking transition (Fig. 7). The phase-field simulations results are in remarkably good quantitative agreement with experiments. The results of the phase-field simulations show that, in absence of fracture energy anisotropy the crack propagates straight in both samples. This is not surprising since both sample geometries and load configurations are symmetric with respect to the horizontal axis and create no mode-II stresses. Consistent with the crack paths shown in Fig. 6, simulations show that crack propagate straight in short samples (see Fig. 14b), but exhibit a smooth transition from straight to kinked propagation in long samples (Fig. 10) with increasing anisotropy. In particular cracks in long sample for $\mathcal{A} > 2.4$ (see Fig. 10) kink sharply upon propagation. The transition from straight propagation to kinked can be understood intuitively in terms of competition between the ability of the crack to release the stored elastic energy and the energetic cost of creating a new surface growing a crack. Since the maximum normal stresses in the specimen are oriented in the y-direction, a crack propagating along the x-axis would release the highest amount of energy. However, the energetic cost of propagating perpendicular to the platelets increases with increasing \mathcal{A} (f_v).

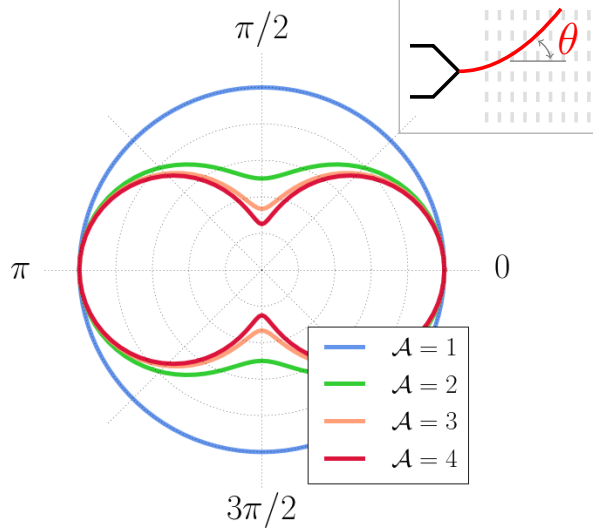


Fig. 9: Polar plots of the fracture energy $\Gamma(\theta) = \Gamma_{\perp} \sqrt{\mathcal{A}^{-2} \sin^2(\theta) + \cos^2(\theta)}$ [31] for different anisotropies \mathcal{A} and θ defined as the angle between the crack propagation axis and a horizontal axis parallel to the parent crack (inset). Plots correspond to the \perp orientation where platelet faces are perpendicular to the parent crack axis.

Therefore, the kinked crack path provides a compromise to balance the cost of propagating in an “easy direction” with smaller amount of energy released.

This transition is further quantified in Fig. 11 where we plot the initial kink angle θ^* as a function \mathcal{A} and superimpose experimental measurements of θ^* using Fig. 8d to relate f_v and \mathcal{A} . This remarkable agreement between the experimental measurements and the phase-field simulations (with isotropic elasticity) establishes the role of fracture energy anisotropy in deflecting the crack. However, the question remains, why the cracks in the short sample propagate straight?

The effect of the sample geometry on crack kinking in different isotropic specimens has been long observed [71, 72, 73, 74, 57] where the crack can kink due to the effect of non-singular stresses around the crack tip. For a crack propagating along the x-axis we can write the near crack tip divergent

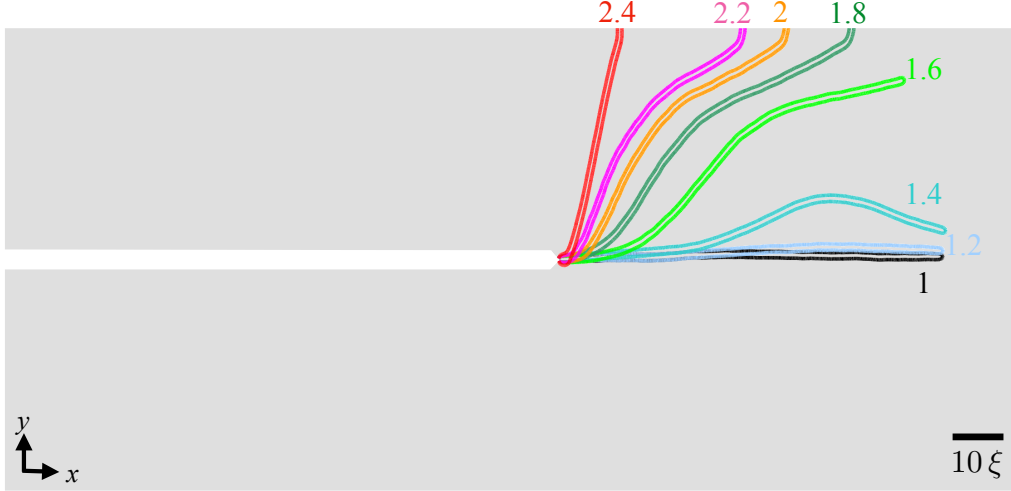


Fig. 10: Phase-field fracture paths for $\xi = 225 \mu\text{m}$ (mirrored to $y > 0$) showing a smooth transition from straight to kinked crack propagation in long samples with increasing fracture energy anisotropy.

stress fields as:

$$\sigma_{xx} = \frac{K_I}{\sqrt{2\pi r}} F_{11}(\theta) + T \quad (16)$$

$$\sigma_{yy} = \frac{K_I}{\sqrt{2\pi r}} F_{21}(\theta) \quad (17)$$

which define the mode-I stress-intensity-factor (SIF) K_I and T-stress T of the crack, where (r, θ) are the polar coordinates centered at the crack tip and F_{ij} have universal forms. In their classic paper, Cotterell and Rice [75] revealed the critical role of the sign of the T-stress on crack path stability by analyzing the smooth trajectory of a curvilinear crack initially perturbed by a small kink angle. Their analysis shows that trajectories deviate exponentially away from the parent crack direction for $T > 0$ (unstable propagation) or return parabolically to this direction for $T < 0$ (stable propagation). However, this calculation conducted in the traditional linear elastic fracture mechanics (LEFM) framework neglects the role of the process zone scale and thus cannot predict the onset of crack kinking in the experiments. While the magnitude of non-singular stress T is generally smaller than the magnitude of

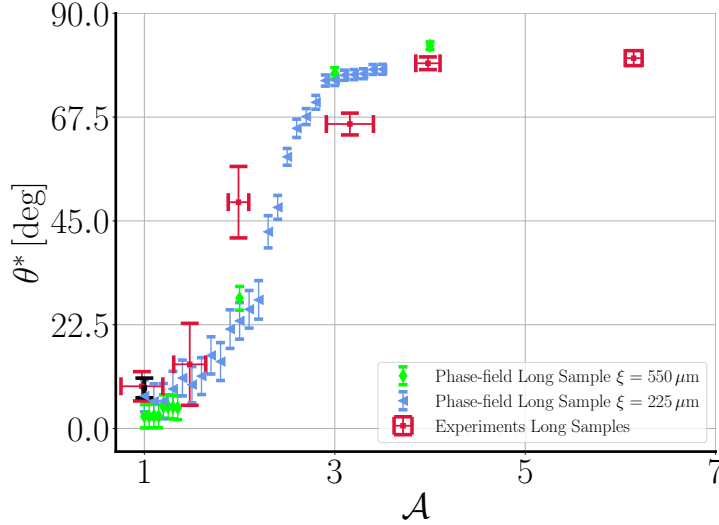


Fig. 11: Comparison of simulated and experimentally observed initial kink angles in long samples. Experiments are for different volume percentages of platelets: $f_v = 0$ (black) and $f_v = 0.01-0.07$ (red) where horizontal and vertical error bars signify the standard error of fracture energy anisotropy (Fig. 8d) and initial kink angle (Fig. 7), respectively. Simulation results are shown for different anisotropies with the associated standard deviation due to discretization for $\xi = 550 \mu\text{m}$ (green triangles) and $\xi = 225 \mu\text{m}$ (blue diamonds).

singular stresses on the process zone scale $\sim K_I/\sqrt{\xi}$, the ratio of non-singular and singular stresses, $T\sqrt{\xi}/K_I$, is appreciable when process zone size is large enough when compared to the sample size. Similar to our results, Ayatollahi et al. [57] showed that for double cantilever beams (DCB) and compact tension (CT) specimens made of (isotropic) PMMA, stability of cracks is affected by the specimen size and geometry through the sign and magnitude of T-stress. In their study, they showed that the crack stability is well predicted by the dimensionless T-stress value $T\sqrt{\xi}/K_I$ for an appropriate choice of the process zone size ξ . For the present experiments in anisotropic media, crack kinking can be predicted quantitatively by phase-field modeling, which phenomenologically regularizes stress field divergences on a scale ξ determined from materials properties and hence inherently captures T-stress effects. It can also be predicted quantitatively in the traditional theoretical framework of LEFM using analytical expressions for the energy release rate that take into account T-stress effects [76]. Results of this analysis will be presented elsewhere. Here we illustrate qualitatively in Fig. 12 how in

phase-field simulations a negative T-stress suppresses kinking by concentrating higher opening stresses along the crack axis (relative to $T = 0$) and a positive T-stress facilitates kinking by spreading opening stresses away from this axis.

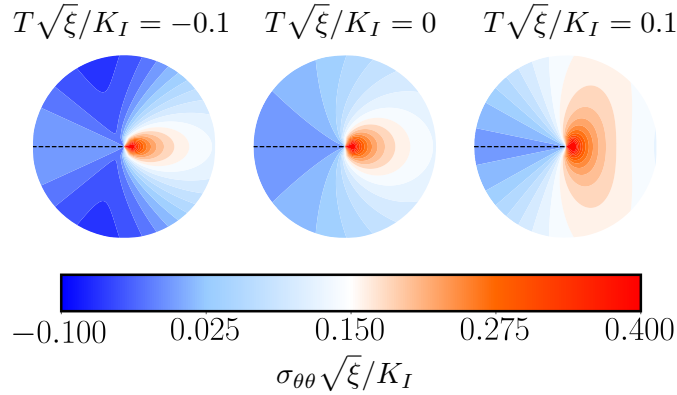


Fig. 12: Contour plots illustrating the influence of the T-stress on the hoop stress $\sigma_{\theta\theta}$ plotted inside a circular domain of radius $r = 10\xi$ centered around the crack tip. Stresses are capped for $r \leq \xi$.

Our experimental and numerical results thus demonstrate that, unlike geometries considered by Ayatollahi et al. [57], in the long sample geometry the geometry effect alone is not enough to destabilize straight propagation. However, the added effect of fracture energy anisotropy can result in the deflection of the crack. On the other hand, while our short sample geometry stabilizes the crack path for small fracture energy anisotropies, we can hypothesize that cracks get deflected for large enough \mathcal{A} . We tested this prediction by repeating a fracture experiment in a short sample for a higher volume fraction ($f_v = 0.1$ corresponding to $\mathcal{A} \simeq 9$) and phase-field simulations. Both experiment Fig. 13a and simulations Fig. 13b produced kinking as predicted, albeit the kinking occurred at a lower threshold in simulations $A \simeq 5.75$ compared to the experiments. We attribute the source of this discrepancy to the approximate form of the fracture energy anisotropy function $\Gamma(\theta)$ used. Despite this discrepancy, we can conclude that the difference in the observed crack paths between long and short sample geometries stems in phase-field simulations from the combination of the process zone size and the sign and magnitude of the T-stress in the two samples. The results suggest

that the same combination is controlling crack path selection in the experiments even though the fracture processes on the process zone scale are only phenomenologically modeled in the phase-field approach.

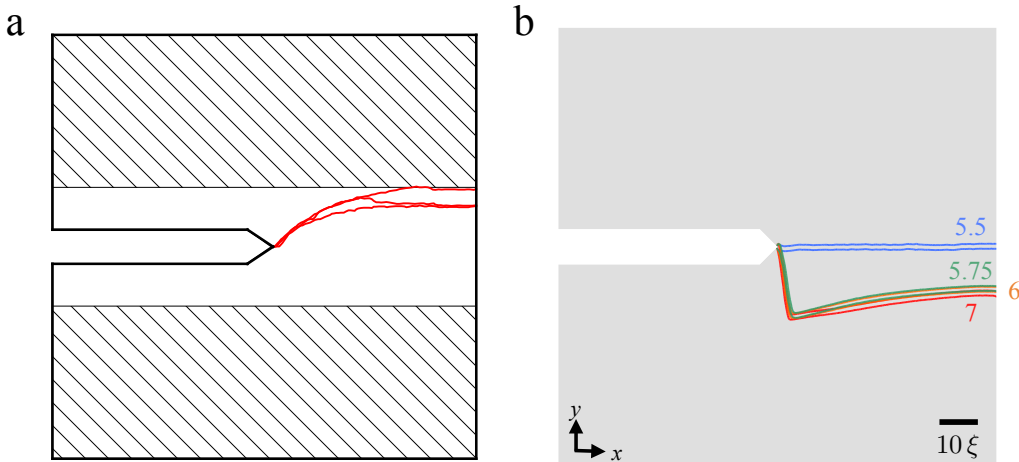


Fig. 13: Crack kinking in the short sample. **a**, Experimental crack path in short sample geometry at 10% volume fraction ($\mathcal{A} \simeq 9$) showing crack kinking. **b**, Results of phase-field simulation in short sample showing transition to kinking at $\mathcal{A} \simeq 5.75$.

3.3. Crack kinking for other platelet orientations

To investigate the effect of sample geometry on crack paths for other orientations than the \parallel and \perp , we carried out a series of experiments and phase-field simulations with varying platelet orientation between 0 and 90 degrees in both the short and long sample geometries. We chose a 4% volume fraction of platelets ($f_v = 0.04$) for which cracks propagate straight in short samples but kink in long samples for $\alpha_\Gamma = 90^\circ$ due to the sample geometry effect. We also performed additional phase-field simulations in both geometries where we assumed that the fracture energy anisotropy rotates precisely with α_Γ . The results are reported in Fig. 14 where we plot the kink angle θ^* as a function of α_Γ (Fig. 14a) and show some examples of computed crack paths in the short sample (Fig. 14b). The results in Fig. 14a show that the kink angle differs significantly between the short and long samples for angles larger than about 45° , thereby demonstrating that the sample geometry strongly affects cracks paths for a wide range of other orientations than the perpendicular one. For $\alpha_\Gamma < 45^\circ$, the geometry effect is small and the crack

path follows approximately the low fracture energy direction ($\theta^* \simeq \alpha_\Gamma$). As previously shown, the crack path propagates straight in the short sample for \parallel and \perp orientations. However, at intermediate angles $0 < \alpha_\Gamma < \pi/2$ the symmetry of the sample versus the x-axis is broken and therefore cracks cannot propagate straight for these platelet orientations. We can further explain the transition cycle from straight propagation to deflection and back, in the short sample geometry, using the phase-field simulations results in Fig. 14. We observe that initially for $\alpha_\Gamma < 60^\circ$ the kink angle θ^* increases with the platelets orientation α_Γ . However, at larger $\alpha_\Gamma > 60^\circ$ (see 80° in Fig. 14b for example) the initial kink occurs at a smaller angle followed by a subsequent straight propagation where the crack path is stabilized as a result of the mode-II loading due to its vertical shift. Simply put, mode-II stresses create a configurational force acting perpendicular to the crack axis that balances out the effect of fracture energy anisotropy which tends to turn the crack axis into a direction that minimizes the surface energy $\Gamma(\theta)$ [31]. The discrepancy of the kink angle θ^* between phase-field simulations and the experimental observation in the short sample highlights the importance of the anisotropy function. In absence of additional measurements of fracture energy anisotropy for the intermediate angles, our choice of the anisotropy function is only a first reasonable estimate that we can partially corroborate by non-trivial prediction of the onset of kinking with increasing platelet volume fraction in long samples ($\mathcal{A}_c \simeq 2$). In future studies, it may be possible to measure the fracture energy for other orientations than \parallel and \perp . Those measurements, however, are difficult because cracks in short samples kink for platelet orientations intermediate orientations. Consequently, the fracture energy cannot be extracted directly from force-displacement curves. This difficulty could be potentially circumvented by imposing mode-II (for example by offsetting the initial notch vertically) to force the crack to propagate straight in a medium of tilted platelets or by using numerical calculations to infer the fracture energy from load-displacement curves for those orientations.

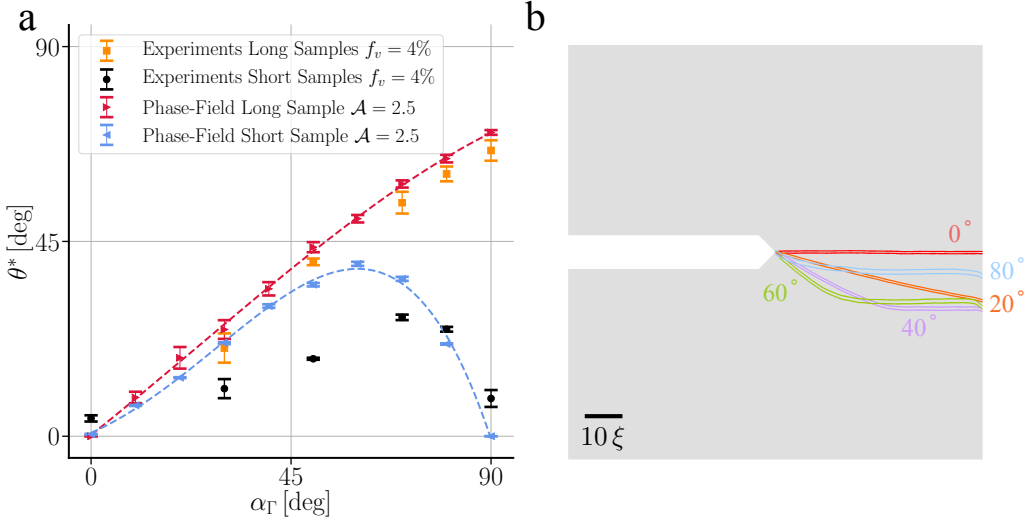


Fig. 14: **a**, Comparison of experimental measurements, and phase-field simulations for the kink angle θ^* as a function of the angle α_Γ between the materials axis corresponding to the lowest fracture energy and the x -axis of the initial crack. The comparison is shown for both short and long 4% ($f_v = 0.04$) samples to highlight the role of the T-stress on crack kinking. In this plot, $\alpha_\Gamma = 0^\circ$ and $\alpha_\Gamma = 90^\circ$ correspond to the \parallel and \perp orientations, respectively. The T-stress is seen to have a strong influence on kinking as seen by the large difference of kink angles in short and long samples for a wide range of angles larger than approximately $\alpha_\Gamma = 45^\circ$. Two values of fracture energy anisotropy $\mathcal{A} = 2.5, 3$ where used to assess the effect of the anisotropy on kinking. **b**, Illustration of crack paths from phase-field simulation results for different α_Γ values in the short samples.

4. Conclusions

Our experimental and numerical results presented in this article highlight the interplay between the fracture energy anisotropy and sample geometry in crack path selection. In this article, we combined experiments and simulations to show that while the crack path remains complex at the microscale, it is controlled at the macroscale by an emergent fracture energy anisotropy. We further, demonstrated both numerically and experimentally that the onset of crack deflection not only depends on the microstructure (*e.g.*, volume fraction and orientation of platelets) but also is strongly influenced by the nonsingular T-stress which is a function of the geometry and loading configuration. Our numerical simulations presented show how the phase-field fracture method can be used in conjunction with the experimental measure-

ment to predict crack path in orientationally ordered composites.

Furthermore, our results suggest that in a natural composite such as bone with a much higher volume fraction of platelets ($f_v \simeq 0.4$), aligned mineralized collagen should suffice to produce crack kinking for propagation perpendicular to fibers independently of the sample geometry as observed experimentally [9], and that straight propagation in pathological bone [10] is due to a dramatic reduction of fracture energy anisotropy (i.e. $\mathcal{A} < \mathcal{A}_c$) caused by fiber misalignment. From a materials engineering standpoint, the strength of polymers reinforced by discontinuous ceramic filler is generally predicted with shear-lag theory in the literature [77], which assumes that the matrix and filler will ultimately fail through yielding and not through the brittle fracture of cracks propagating from defects. This treatment infers that composites are flaw tolerant during failure, a feature that is in potential disagreement with the low fracture energy exhibited by many ceramic filled polymer systems. In the current material system, for example, 5% samples have order of a millimeter critical flaw sizes, suggesting that the crack geometries tested in this work reside in the brittle fracture regime and that shear-lag theory would over predict their performance. This understanding should help interpret fracture experiments in a wide range of composites.

5. Acknowledgements

This research was supported by NSF grant CMMI-1536354. The majority of the numerical simulations presented in this work were performed using resources of the Extreme Science and Engineering Discovery Environment (XSEDE) under the resource allocation TG-MSS160013. The remainder of the simulations benefited from computing time allocation on Northeastern University’s Discovery Cluster at the Massachusetts Green High Performance Computing Center (MGHPCC).

6. Author contributions

A.M. and C.P. are co-first authors listed in alphabetical order. A.K., S.J.S., and R.M.E. conceived the research. A.M. and C.P. carried out the computational and experimental studies, respectively. A.M. and A.K. carried out the theoretical analyses. The paper was written with input from all authors.

References

- [1] Ming-Yuan He and John W Hutchinson. Kinking of a crack out of an interface. *Journal of Applied Mechanics*, 56(2):270–278, 1989.
- [2] B. K. Ahn, W. A. Curtin, T. A. Parthasarathy, and R. E. Dutton. Criteria for crack deflection/penetration criteria for fiber-reinforced ceramic matrix composites. *Composites Science and Technology*, 58(11):1775–1784, 1998.
- [3] Harika C. Tankasala, Vikram S. Deshpande, and Norman A. Fleck. Crack kinking at the tip of a mode i crack in an orthotropic solid. *International Journal of Fracture*, 207(2):181–191, Jul 2017.
- [4] F Barthelat and HD Espinosa. An experimental investigation of deformation and fracture of nacre–mother of pearl. *Experimental mechanics*, 47(3):311–324, 2007.
- [5] Robert O Ritchie. The conflicts between strength and toughness. *Nature materials*, 10(11):817, 2011.
- [6] Dipanjan Sen and Markus J Buehler. Structural hierarchies define toughness and defect-tolerance despite simple and mechanically inferior brittle building blocks. *Scientific reports*, 1:35, 2011.
- [7] Leon S Dimas, Graham H Bratzel, Ido Eylon, and Markus J Buehler. Tough composites inspired by mineralized natural materials: computation, 3d printing, and testing. *Advanced Functional Materials*, 23(36):4629–4638, 2013.
- [8] M Mirkhalaf, A Khayer Dastjerdi, and F Barthelat. Overcoming the brittleness of glass through bio-inspiration and micro-architecture. *Nature communications*, 5:3166, 2014.
- [9] K. J. Koester, J. W. Ager, and R. O. Ritchie. The true toughness of human cortical bone measured with realistically short cracks. *Nat Mater*, 7(8):672–677, 08 2008.
- [10] Alessandra Carriero, Elizabeth A Zimmermann, Adriana Paluszny, Simon Y Tang, Hrishikesh Bale, Bjorn Busse, Tamara Alliston, Galateia

- Kazakia, Robert O Ritchie, and Sandra J Shefelbine. How tough is brittle bone? investigating osteogenesis imperfecta in mouse bone. *Journal of Bone and Mineral Research*, 29(6):1392–1401, 2014.
- [11] Nobphadon Suksangpanya, Nicholas A Yaraghi, R Byron Pipes, David Kisailus, and Pablo Zavattieri. Crack twisting and toughening strategies in bouligand architectures. *International Journal of Solids and Structures*, 150:83–106, 2018.
- [12] Marc André Meyers, Albert Yu-Min Lin, Po-Yu Chen, and Julie Muyco. Mechanical strength of abalone nacre: Role of the soft organic layer. *Journal of the Mechanical Behavior of Biomedical Materials*, 1(1):76–85, 1 2008.
- [13] Zaiwang Huang and Xiaodong Li. Origin of flaw-tolerance in nacre. *Scientific reports*, 3, 2013.
- [14] Navid Sakhavand and Rouzbeh Shahsavari. Universal composition–structure–property maps for natural and biomimetic platelet–matrix composites and stacked heterostructures. *Nat Commun*, 6, 03 2015.
- [15] H. Schachner, A. Reiterer, and S. E. Stanzl-Tschegg. Orthotropic fracture toughness of wood. *Journal of Materials Science Letters*, 19(20):1783–1785, 2000.
- [16] Shigeyasu Amada and Sun Untao. Fracture properties of bamboo. *Composites Part B: Engineering*, 32(5):451–459, 2001.
- [17] Sabine Bechtle, Stefan Habelitz, Arndt Klocke, Theo Fett, and Gerold A Schneider. The fracture behaviour of dental enamel. *Biomaterials*, 31(2):375–384, 2010.
- [18] Richard G Hoagland, George T Hahn, and Alan R Rosenfield. Influence of microstructure on fracture propagation in rock. *Rock mechanics*, 5(2):77–106, 1973.
- [19] Michael R Chandler, Philip G Meredith, Nicolas Brantut, and Brian R Crawford. Fracture toughness anisotropy in shale. *Journal of Geophysical Research: Solid Earth*, 121(3):1706–1729, 2016.

- [20] Vellore S. Gopalaratnam and Ravindra Gettu. On the characterization of flexural toughness in fiber reinforced concretes. *Cement and Concrete Composites*, 17(3):239–254, 1995.
- [21] Feiyu Yang, Xinghong Zhang, Jiecai Han, and Shanyi Du. Mechanical properties of short carbon fiber reinforced zrb₂-sic ceramic matrix composites. *Materials Letters*, 62(17):2925–2927, 2008.
- [22] Jian Liu, Haixue Yan, and Kyle Jiang. Mechanical properties of graphene platelet-reinforced alumina ceramic composites. *Ceramics International*, 39(6):6215–6221, 2013.
- [23] Byung Chul Kim, Sang Wook Park, and Dai Gil Lee. Fracture toughness of the nano-particle reinforced epoxy composite. *Composite Structures*, 86(1):69–77, 2008.
- [24] Florian Bouville, Eric Maire, Sylvain Meille, Bertrand Van de Moortèle, Adam J. Stevenson, and Sylvain Deville. Strong, tough and stiff bioinspired ceramics from brittle constituents. *Nature Materials*, 13:508 EP –, 03 2014.
- [25] Joshua J. Martin, Brad E. Fiore, and Randall M. Erb. Designing bioinspired composite reinforcement architectures via 3d magnetic printing. *Nature Communications*, 6:8641 EP –, 10 2015.
- [26] S. Keck and M. Fulland. Effect of fibre volume fraction and fibre direction on crack paths in flax fibre-reinforced composites. *Engineering Fracture Mechanics*, 167:201–209, 2016.
- [27] Paul O. Judt, Jan-Christoph Zarges, Maik Feldmann, Andreas Ricoeur, and Hans-Peter Heim. Deflecting mode-i cracks in anisotropic materials. *Mechanics of Materials*, 136:103060, 2019.
- [28] G.A. Francfort and J.J. Marigo. Revisiting brittle fracture as an energy minimization problem. *Journal of the Mechanics and Physics of Solids*, 46(8):1319–1342, 1998.
- [29] Alain Karma, David A. Kessler, and Herbert Levine. Phase-field model of mode iii dynamic fracture. *Phys. Rev. Lett.*, 87:045501, Jul 2001.

- [30] B. Bourdin, G. A. Francfort, and J.-J. Marigo. The variational approach to fracture. *Journal of Elasticity*, 91(1):5–148, 2008.
- [31] Vincent Hakim and Alain Karma. Laws of crack motion and phase-field models of fracture. *Journal of the Mechanics and Physics of Solids*, 57(2):342–368, 2 2009.
- [32] A. Mesgarnejad, B. Bourdin, and M. M. Khonsari. Validation simulations for the variational approach to fracture mechanics. *Computer Methods in Applied Mechanics and Engineering*, 2015.
- [33] A. Mesgarnejad, B. Bourdin, and M. M. Khonsari. A variational approach to the fracture of brittle thin films subject to out-of-plane loading. *Journal of mechanics and physics of solids*, 61(11):2360–2379, November 2013.
- [34] B. Bourdin, J.-J. Marigo, C. Maurini, and P. Sicsic. Morphogenesis and propagation of complex cracks induced by thermal shocks. *Phys. Rev. Lett.*, 112:014301, Jan 2014.
- [35] Chih-Hung Chen, Tristan Cambonie, Veronique Lazarus, Matteo Nicoli, Antonio J. Pons, and Alain Karma. Crack front segmentation and facet coarsening in mixed-mode fracture. *Phys. Rev. Lett.*, 115:265503, Dec 2015.
- [36] C. Miehe, H. Dal, and A. Raina. A phase field model for chemo-mechanical induced fracture in lithium-ion battery electrode particles. *International Journal for Numerical Methods in Engineering*, pages n/a–n/a, 2015.
- [37] P. Zuo and Y.-P. Zhao. A phase field model coupling lithium diffusion and stress evolution with crack propagation and application in lithium ion batteries. *Physical Chemistry Chemical Physics*, 17(1):287–297, 2015.
- [38] M. Klinsmann, D. Rosato, M. Kamlah, and R. M. McMeeking. Modeling crack growth during li extraction in storage particles using a fracture phase field approach. *Journal of The Electrochemical Society*, 163(2):A102–A118, 01 2016.

- [39] Markus Klinsmann, Daniele Rosato, Marc Kamlah, and Robert M. McMeeking. Modeling crack growth during li insertion in storage particles using a fracture phase field approach. *Journal of the Mechanics and Physics of Solids*, 92:313–344, 7 2016.
- [40] Chih-Hung Chen, Eran Bouchbinder, and Alain Karma. Instability in dynamic fracture and the failure of the classical theory of cracks. *Nat Phys*, 13:1186–1190, 08 2017.
- [41] Yuri Lubomirsky, Chih-Hung Chen, Alain Karma, and Eran Bouchbinder. Universality and stability phase diagram of two-dimensional brittle fracture. *Physical review letters*, 121(13):134301, 2018.
- [42] C. Peco, Y. Liu, C. Rhea, and J. E. Dolbow. Models and simulations of surfactant-driven fracture in particle rafts. *International Journal of Solids and Structures*, 156-157:194–209, 2019.
- [43] N. Mozaffari and G. Z. Voyiadjis. Phase field based nonlocal anisotropic damage mechanics model. *Physica D: Nonlinear Phenomena*, 308:11–25, 7 2015.
- [44] M. Ambati, T. Gerasimov, and L. De Lorenzis. Phase-field modeling of ductile fracture. pages 1–24, 2015.
- [45] Michael J Borden, Thomas JR Hughes, Chad M Landis, Amin Anvari, and Isaac J Lee. A phase-field formulation for fracture in ductile materials: Finite deformation balance law derivation, plastic degradation, and stress triaxiality effects. *Computer Methods in Applied Mechanics and Engineering*, 2016.
- [46] Roberto Alessi, Jean-Jacques Marigo, Corrado Maurini, and Stefano Vidoli. Coupling damage and plasticity for a phase-field regularisation of brittle, cohesive and ductile fracture: one-dimensional examples. *International Journal of Mechanical Sciences*, pages –, 2017.
- [47] Roberto Alessi, Stefano Vidoli, and Laura De Lorenzis. A phenomenological approach to fatigue with a variational phase-field model: The one-dimensional case. *Engineering Fracture Mechanics*, 190:53–73, 2018.

- [48] P Carrara, M Ambati, R Alessi, and L De Lorenzis. A novel framework to model the fatigue behavior of brittle materials based on a variational phase-field approach. *arXiv preprint arXiv:1811.02244*, 2018.
- [49] A. Mesgarnejad, A. Imanian, and A. Karma. Phase-field models for fatigue crack growth. *Theoretical and Applied Fracture Mechanics*, page 102282, 2019.
- [50] Vincent Hakim and Alain Karma. Crack path prediction in anisotropic brittle materials. *Physical review letters*, 95(23):235501, 2005.
- [51] Bin Li, Christian Peco, Daniel Millán, Irene Arias, and Marino Arroyo. Phase-field modeling and simulation of fracture in brittle materials with strongly anisotropic surface energy. *International Journal for Numerical Methods in Engineering*, 102(3-4):711–727, 2015.
- [52] Palla Murali, Tanmay K Bhandakkar, Wei Li Cheah, Mark H Jhon, Huajian Gao, and Rajeev Ahluwalia. Role of modulus mismatch on crack propagation and toughness enhancement in bioinspired composites. *Physical Review E*, 84(1):015102, 2011.
- [53] Mohammed A. Msekh, M. Silani, M. Jamshidian, P. Areias, X. Zhuang, G. Zi, P. He, and Timon Rabczuk. Predictions of j integral and tensile strength of clay/epoxy nanocomposites material using phase field model. *Composites Part B: Engineering*, 93:97–114, 2016.
- [54] Congjie Wei, Chenglin Wu, and Charles Wojnar. Effect of patterned inclusions on the fracture behavior of ceramic composites. *Composites Part B: Engineering*, 172:564–592, 2019.
- [55] Duc Hong Doan, Tinh Quoc Bui, Nguyen Dinh Duc, and Kazuyoshi Fushinobu. Hybrid phase field simulation of dynamic crack propagation in functionally graded glass-filled epoxy. *Composites Part B: Engineering*, 99:266–276, 2016.
- [56] Hirshikesh, Sundararajan Natarajan, Ratna K. Annabattula, and Emilio Martínez-Pañeda. Phase field modelling of crack propagation in functionally graded materials. *Composites Part B: Engineering*, 169:239–248, 2019.

- [57] MR Ayatollahi, M Rashidi Moghaddam, SMJ Razavi, and F Berto. Geometry effects on fracture trajectory of pmma samples under pure mode-i loading. *Engineering Fracture Mechanics*, 163:449–461, 2016.
- [58] LabVIEW User Manual. National instruments. *Austin, TX*, 1998.
- [59] Curtis T. Rueden, Johannes Schindelin, Mark C. Hiner, Barry E. DeZonia, Alison E. Walter, Ellen T. Arena, and Kevin W. Eliceiri. Imagej2: Imagej for the next generation of scientific image data. *BMC Bioinformatics*, 18(1):529, 2017.
- [60] Itamar Kolvin, Gil Cohen, and Jay Fineberg. Topological defects govern crack front motion and facet formation on broken surfaces. *Nature materials*, 17(2):140, 2018.
- [61] Haocheng Quan, Wen Yang, Eric Schaible, Robert O. Ritchie, and Marc A. Meyers. Novel defense mechanisms in the armor of the scales of the “living fossil” coelacanth fish. *Advanced Functional Materials*, 28(46):1804237, Sep 2018.
- [62] B. S. Kirk, Peterson J. W., Stogner R. H., and Carey G. F. libMesh: A C++ Library for Parallel Adaptive Mesh Refinement/Coarsening Simulations. *Engineering with Computers*, 22(3–4):237–254, 2006.
- [63] S. Balay, W. D. Gropp, L. C. McInnes, and B. F. Smith. Efficient management of parallelism in object oriented numerical software libraries. In E. Arge, A. M. Bruaset, and H. P. Langtangen, editors, *Modern Software Tools in Scientific Computing*, pages 163–202. Birkhäuser Press, 1997.
- [64] Satish Balay, Shrirang Abhyankar, Mark F. Adams, Jed Brown, Peter Brune, Kris Buschelman, Lisandro Dalcin, Victor Eijkhout, William D. Gropp, Dinesh Kaushik, Matthew G. Knepley, Dave A. May, Lois Curfman McInnes, Karl Rupp, Patrick Sanan, Barry F. Smith, Stefano Zampini, Hong Zhang, and Hong Zhang. PETSc users manual. Technical Report ANL-95/11 - Revision 3.8, Argonne National Laboratory, 2017.
- [65] S Kamat, X Su, R Ballarini, and AH Heuer. Structural basis for the fracture toughness of the shell of the conch strombus gigas. *Nature*, 405(6790):1036, 2000.

- [66] Min Kyoon Shin, Bommy Lee, Shi Hyeong Kim, Jae Ah Lee, Geoffrey M. Spinks, Sanjeev Gambhir, Gordon G. Wallace, Mikhail E. Kozlov, Ray H. Baughman, and Seon Jeong Kim. Synergistic toughening of composite fibres by self-alignment of reduced graphene oxide and carbon nanotubes. *Nature Communications*, 3:650 EP –, 01 2012.
- [67] Pertti Auerkari. *Mechanical and physical properties of engineering alumina ceramics*. 1996.
- [68] Kim Pham, Jean-Jacques Marigo, et al. Damage localization and rupture with gradient damage models. *Fracture and Structural Integrity*, 19, 2012.
- [69] Kim Pham and Jean-Jacques Marigo. From the onset of damage to rupture: construction of responses with damage localization for a general class of gradient damage models. *Continuum Mechanics and Thermo-dynamics*, pages 1–25, 2013.
- [70] Zdeněk P Bažant. Scaling theory for quasibrittle structural failure. *Proceedings of the National Academy of Sciences of the United States of America*, 101(37):13400–13407, 2004.
- [71] B Cotterell. On brittle fracture paths. *International Journal of Fracture Mechanics*, 1(2):96–103, 1965.
- [72] B. Cotterell. On fracture path stability in the compact tension test. *International Journal of Fracture*, 6(2):189–192, 1970.
- [73] DJ Smith, MR Ayatollahi, and MJ Pavier. The role of t-stress in brittle fracture for linear elastic materials under mixed-mode loading. *Fatigue & Fracture of Engineering Materials & Structures*, 24(2):137–150, 2001.
- [74] DJ Smith, MR Ayatollahi, and MJ Pavier. On the consequences of t-stress in elastic brittle fracture. *Proceedings of the Royal Society A: Mathematical, Physical and Engineering Sciences*, 462(2072):2415–2437, 2006.
- [75] B. Cotterell and J.R. Rice. Slightly curved or kinked cracks. *International Journal of Fracture*, 16(2):155–169, 1980.

- [76] M. Amestoy and J. B. Leblond. Crack paths in plane situations—ii. detailed form of the expansion of the stress intensity factors. *International Journal of Solids and Structures*, 29(4):465–501, 1992.
- [77] Lorenz J. Bonderer, AndréR. Studart, and Ludwig J. Gauckler. Bioinspired design and assembly of platelet reinforced polymer films. *Science*, 319(5866):1069, 02 2008.